Article

SOURCE DATA | TRANSPARENT PROCESS

EMBO reports

Slit-Robo signalling establishes a Sphingosine-1-phosphate gradient to polarise fin mesenchyme

Harsha Mahabaleshwar[1,†], PV Asharani[2,†], Tricia Yi Loo[3], Shze Yung Koh[1], Melissa R Pitman[4,5], Samuel Kwok[1], Jiajia Ma[1], Bo Hu[6], Fang Lin[6], Xue Li Lok[2], Stuart M Pitson[4], Timothy E Saunders[2,3,7] & Tom J Carney[1,2,*]

Abstract

Immigration of mesenchymal cells into the growing fin and limb buds drives distal outgrowth, with subsequent tensile forces between these cells essential for fin and limb morphogenesis. Morphogens derived from the apical domain of the fin, orientate limb mesenchyme cell polarity, migration, division and adhesion. The zebrafish mutant *stomp* displays defects in fin morphogenesis including blister formation and associated loss of orientation and adhesion of immigrating fin mesenchyme cells. Positional cloning of *stomp* identifies a mutation in the gene encoding the axon guidance ligand, Slit3. We provide evidence that Slit ligands derived from immigrating mesenchyme act via Robo receptors at the apical ectodermal ridge (AER) to promote release of sphingosine-1-phosphate (S1P). S1P subsequently diffuses back to the mesenchyme to promote their polarisation, orientation, positioning and adhesion to the interstitial matrix of the fin fold. We thus demonstrate the coordination of the Slit-Robo and S1P signalling pathways in fin fold morphogenesis. Our work introduces a mechanism regulating the orientation, positioning and adhesion of its constituent cells.

Keywords fin; mesenchyme; Robo; Slit; sphingosine-1-phosphate
Subject Categories Cell Adhesion, Polarity & Cytoskeleton; Development; Signal Transduction
DOI 10.15252/embr.202154464 | Received 7 December 2021 | Revised 12 May 2022 | Accepted 18 May 2022 | Published online 9 June 2022
EMBO Reports (2022) 23: e54464
See also: **IM Sehring & G Weidinger** (August 2022)

Introduction

During limb formation, anisotropic growth along the proximal–distal axis results in a flat, paddle-shaped limb bud. How signalling between constituent cells and the biophysical properties of the forming limb are coordinated to attain this morphology has attracted much speculation (Hopyan *et al*, 2011). Limb bud mesenchyme migration, morphology and adhesion are highly polarised through apical ectodermal ridge (AER)-derived signals, including Wnt5a (Gros *et al*, 2010). This results in filopodial protrusions which orientate radially towards the ectoderm, with a distal bias, and directs polarised orientation, cell division and convergent extension, and thus orientated limb outgrowth (Wyngaarden *et al*, 2010; Hopyan *et al*, 2011). Furthermore, both tensional forces and a distal–proximal gradient of cell adhesiveness along the limb bud also regulate limb morphogenesis (Wada, 2011; Lau *et al*, 2015). It is important to understand the processes driving mesodermal cell polarisation, migration and organisation in the limb, and the biophysical properties they impart.

The limb mesenchyme can exert morphogenetic tension on the limb bud extracellular matrix (ECM) through contractility (Oster *et al*, 1983; Martin & Lewis, 1986). Furthermore, the migration of limb mesenchyme has been proposed to be influenced by haptotactic forces (Oster *et al*, 1983), although this has not been demonstrated *in vivo*. A range of diverse cues alter the adhesive and contractile properties of mesenchymal cells. The soluble phospholipid, sphingosine-1-phosphate (S1P) promotes cell migration, adhesiveness and myosin-based contractile tension in mesenchymal cells and fibroblasts (Wang *et al*, 1997; Hobson *et al*, 2001; Kanazawa *et al*, 2010; Hinz, 2016). S1P signals through G-protein-coupled receptors (S1PR1–5), which activate intracellular signalling effectors, including Rho GTPase via the heterotrimeric G-protein $G\alpha_{12/13}$ (Wang *et al*, 1997; Lee *et al*, 1998). S1P levels are regulated by dedicated kinases (SPHK1 and SPHK1) or phosphatases (SPP1 and SPP2) (Pitson, 2011), while S1P is secreted from source cells by Spinster2 (Spns2) homologues (Osborne *et al*, 2008). The pathways defining the regulation of intra- and extracellular S1P levels are not fully elucidated.

1 Lee Kong Chian School of Medicine, Experimental Medicine Building, Nanyang Technological University, Singapore City, Singapore
2 Institute of Molecular and Cell Biology (IMCB), A*STAR (Agency for Science, Technology and Research), Singapore City, Singapore
3 Mechanobiology Institute, National University of Singapore, Singapore City, Singapore
4 Centre for Cancer Biology, University of South Australia, and SA Pathology, North Tce, Adelaide, SA, Australia
5 School of Biological Sciences, University of Adelaide, Adelaide, South Australia, Australia
6 Department of Anatomy & Cell Biology, Carver College of Medicine, The University of Iowa, Iowa City, IA, USA
7 Warwick Medical School, University of Warwick, Coventry, UK
*Corresponding author. Tel: +65 69047045; E-mail: tcarney@ntu.edu.sg
†These authors contributed equally to this work

The importance of S1P in regulating cell behaviour and morphogenesis is demonstrated in zebrafish mutants for *s1pr2*, *spns2* and *MZsphk2*, which all display cardia bifida, and highlight a role for extracellular S1P in endoderm and cardiac mesoderm migration (Kupperman *et al*, 2000; Osborne *et al*, 2008; Mendelson *et al*, 2015). In addition, these mutants all display larval fin blistering, affecting both pectoral and caudal medial fins through an undefined mechanism.

Here, we characterise the zebrafish mutant, *stompy* (*sto*), which shows blisters within the fin folds, similar to those seen in S1P pathway mutants. Surprisingly, *sto* corresponded to mutations in the secreted axon guidance protein, Slit3. We show that Slit-Robo signalling is required for S1P potency in the fin fold and that S1P acts to polarise immigrating fin mesenchyme, altering their adhesive and migratory behaviour. We show that these results are consistent with a haptotactic model of directed fin mesenchyme migration. Hence, Slit-Robo and S1P coordinate to provide tension to the interstitial matrix of the fin, thus driving robust tissue morphogenesis.

Results

stompy mutant displays blisters in the caudal and pectoral fins

The *stompy* mutant was previously described as having variable degeneration of the pectoral fins (van Eeden *et al*, 1996). However, we noted this degeneration was preceded by formation of blisters in the pectoral fin fold (Fig 1A–D). We also observed small blisters in the caudal median fin in 40% of *sto* mutant embryos, suggesting that *sto* affects all larval fins, as per other fin blister mutants (Fig 1E and F; Carney *et al*, 2010). We noted that the penetrance of the *sto* phenotype was variable (Appendix Table S1) as was expressivity, with 30% of *sto* mutants showing only unilateral pectoral fin blistering. H&E staining of coronal sections through the medial fin (Fig 1G and H) highlighted that blisters form in the proximal portion. The blisters form below the Laminin-positive basement membrane (Fig 1 I and J), similar to that of Fraser complex mutants (Carney *et al*, 2010). However, in contrast to the Fraser mutants, there was no loss of Fras1 protein at the basement membrane of blisters in *stompy* mutants (Fig 1K and L). The blisters that form in the fins of *sto* mutants are transient and collapse during later fin fold growth. We conclude that *stompy* represents a novel component required for fin integrity.

The *stompy* locus encodes *slit3*

We mapped *sto* to Linkage Group 14, refining to an interval containing 11 genes (Appendix Fig S1A). Sequencing the coding region and intron–exon boundaries of 10 of these genes showed no plausible genetic lesion. However, a T to A transversion was found in seven bases upstream of the intron 9–exon 10 splice site of the *slit3* gene (NM_131736; c.1341-7T>A; Appendix Fig S1B and D). This was predicted to generate a novel splice acceptor, and sequencing *slit3* from *sto* mutant cDNA showed inclusion of five nucleotides from the end of intron 9 in the mature mRNA with the frame shift introducing eight erroneous amino acids followed by a premature stop codon (c. 1340_1341insTGTAG; Appendix Fig S1C and D). This truncates the 1516aa Slit3 protein at 305aa (Fig 1M). We noted that the new cryptic splice acceptor was not strong and sequence of *slit3* cDNA from homozygous *sto* mutants showed a mix of aberrant and correctly spliced transcripts. Therefore, to confirm that the loss of Slit3 was responsible for fin blistering, we injected a translation blocking morpholino against *slit3* into wild-type (WT) embryos, which showed blistering in both the caudal fin and pectoral fins (Fig EV1A–C). Additionally, we used TALENs to create a frame-shifting indel mutation in exon 8 (Appendix Fig S1E and F), which is predicted to lead a premature stop codon (*slit3*^{sq49}; Fig 1M). This allele failed to complement *sto*, and 112 of 273 zygotic mutants of this allele showed tail blisters (Fig 1N and O). Hereafter, *stompy* mutants will be labelled as *slit3*$^{-/-}$ mutants.

RT–PCR showed *slit3* is expressed at all stages through to adulthood, including at the two-cell stage indicating maternal contribution (Fig EV1D). We confirmed these observations by *in situ* hybridisation (Fig EV1E and F). We generated maternal zygotic *slit3* mutants and these had more severe tail fin blisters than zygotic *slit3*^{sq49} mutants (Fig 1P). *In situ* hybridisation localised *slit3* expression to the proximal mesoderm region of both the tail and pectoral fins, from which the immigrating mesenchyme originates (Figs 1Q and R, and EV1G and H; Lee *et al*, 2013). We also observed expression of *slit1a* in the larval tail and pectoral fins. *slit1a* expression remained in this population after invading the fin, whereas *slit3* was not expressed in the migrating mesenchyme (Figs 1S–U and EV1I and J). Neither *slit1b* nor *slit2* was expressed in the posterior mesoderm of the tail which gives rise to the fin mesenchyme, although there was some expression of *slit2* in the proximal pectoral fin (Fig EV1K–N). We generated *slit1a* mutants through CRISPR/Cas9-mediated mutagenesis (*slit1a*^{sq51}; Fig EV1O–R). Incrosses of *slit1a* heterozygotes gave 22.5% larvae with strong fin blisters at 48 hpf (Fig 1V). Double *slit1a; slit3* zygotic mutants had more severe blisters compared to either mutant, indicating functional redundancy (Figs 1W and EV1S), while *slit1a*$^{+/-}$ crossed to *slit3*$^{+/-}$ gave clutches with 17.7% (n = 388) of larvae having blisters.

Robo receptors are required for Slit3-mediated fin morphogenesis

Slit proteins signal through Robo receptors and also bind a number of ECM components (Hu, 2001; Xiao *et al*, 2011). *In situ* hybridisation revealed that Robo receptors are expressed in the fin fold, in a complementary pattern to that of the Slit ligands, with all three *robo* receptor genes (*robo1*, *robo2* and *robo3*), dynamically expressed in the apical and sub-apical ectodermal ridge cells of the developing fin folds at different stages (Figs 2A–H and EV2A–G). Subsequently, we investigated fin morphology in zebrafish *robo* receptor gene mutants. We observed mild blistering at 72 hpf in the pectoral fin of embryos injected with a *robo1* morpholino (MO) (Fig EV2H and I). This prompted us to generate a TALEN-mediated knockout of *robo1* (*robo1*^{sq50}; Figs 2I and EV2J–L). Although 13 of 28 (46%) *robo1* mutants also had mild pectoral fin blistering at 72 hpf, there was no apparent tail fin blistering either alone or combined with *robo3*^{tx209} mutants (=*twitch twice*; Burgess *et al*, 2009) (Fig 2J). Similarly, *robo2* ^{te284} (= *astray* mutants) (Fricke *et al*, 2001), or *robo2* ^{te284}; *robo3*^{tx209} double mutants, showed no fin defect (Fig 2K; n = 137). As the *robo1* and *robo2* genes are closely linked to make triple deficient embryos, we resorted to injection of *robo2* or *robo1* morpholinos into *robo1;robo3* or *robo2;robo3* double mutants respectively.

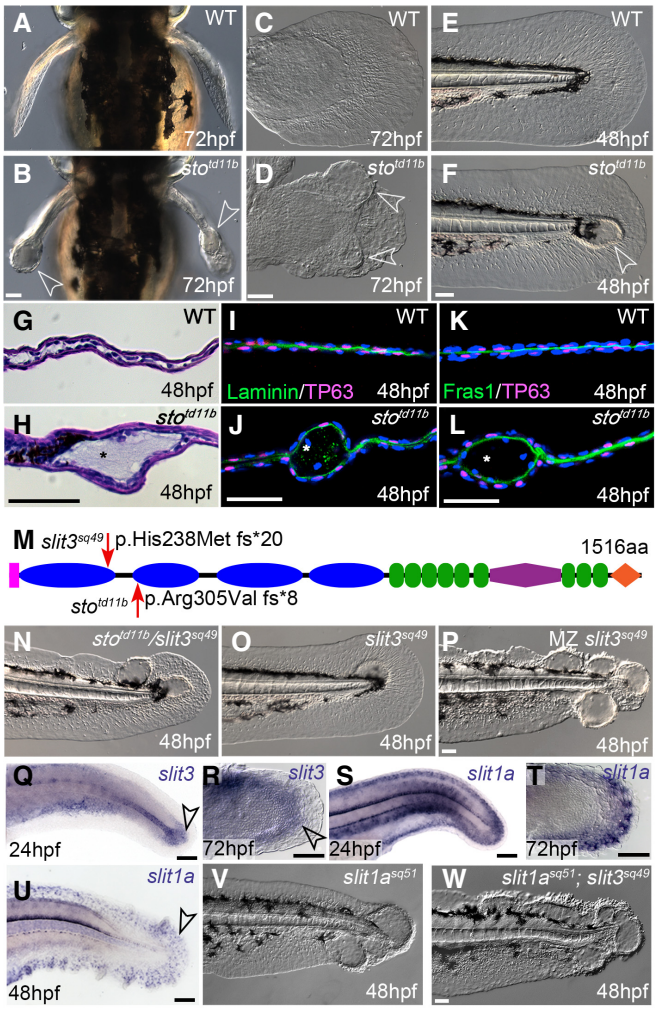

Figure 1. The *stomp* fin blister mutant corresponds to mutations in *slit3*.

A–F Dorsal (A, B) and lateral (C–F) images of the 3 dpf pectoral (A–D) and 2 dpf tail fins (E, F) of WT (A, C, E) and sto^{td11b} homozygous mutants (B, D, F). Open arrowheads indicate blisters.

G, H H&E staining of coronal cryosections through the tail fin region of WT (G) and sto^{td11b} mutant (H) embryos at 2 dpf.

I–L Coronal confocal sections of tail fins from 2 dpf WT (I, K) and sto^{td11b} mutants (J, L), immunostained for TP63 (I–L; magenta), Laminin (I, J; green) or Fras1 (K, L; green) and counterstained with DAPI (blue). Asterisks indicate blister cavity, which is below TP63-positive basal keratinocytes and basement membrane labelled with Laminin and Fras1.

M Schematic of the zebrafish Slit3 protein, indicating the signal peptide (pink), four N-terminal domains with leucine-rich repeats (LRR, blue), six EGF-like domains (green), a lamininG domain (purple), three EGF-like repeats (green) and a C-terminal cysteine-rich knot (orange). Location and nature of the sto^{td11b} ENU and $slit3^{sq49}$ TALEN alleles are indicated at red arrows.

N–P Lateral Nomarski images of $slit3^{td11b/sq49}$ compound heterozygous (N), zygotic $slit3^{sq49}$ homozygous (O) and Maternal-zygotic (*MZ*) $slit3^{sq49}$ (P) tail fins at 48 hpf.

Q–U Lateral bright-field images of tail (Q, S, U) and pectoral (R, T) fins stained by whole mount *in situ* hybridisation for *slit3* (Q, R) and *slit1a* (S–U), indicating expression in proximal mesenchyme (arrowheads).

V, W Lateral Nomarski images of the $slit1a^{sq51}$ mutant (V) and $slit1a^{sq51}$; $slit3^{sq49}$ double-mutant (W) tail fins at 48 hpf, indicating partial redundancy of Slit1a and Slit3 in tail fin morphogenesis.

Data information: Scale bars: 50 μm.

Pronounced epidermal blistering was observed in both cases (Fig 2L and M). Of 154 embryos from a $robo2^{+/-}$; $robo3^{+/-}$ incross, injected with *robo1* MO, 10 had severe blisters (6.5%) while 25 had mild blisters (16%). This indicates that Slit proteins function through their canonical receptors in maintaining integrity of the forming fin and that there is redundancy among Robo receptors in this function. As the only common expression domain of all three Robo receptors is the AER, we conclude that Slits within the developing fin fold are signalling to the AER cells.

Slit-Robo pathway synergises with S1P signalling

We hypothesised that Slit3 acts with other pathways known to cause fin blistering. We previously showed that Fras1 immunoreactivity is

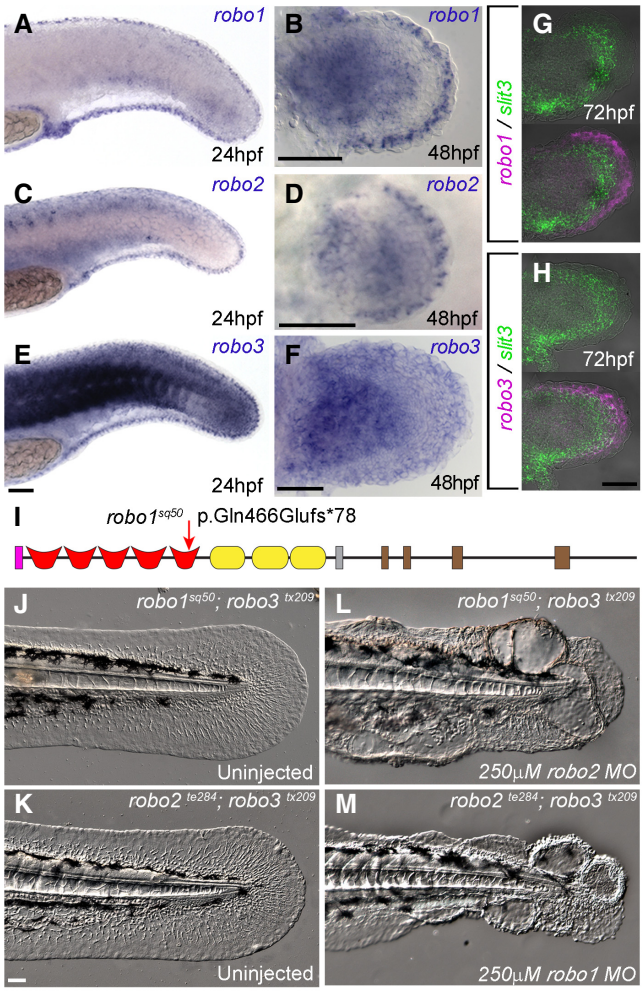

Figure 2. Robo receptors are expressed in the AER cells and act redundantly in fin morphogenesis.

A–F *In situ* hybridisation of tail (A, C, E) and pectoral (B, D, F) fins at 24 and 48 hpf, using probes for *robo1* (A, B), *robo2* (C, D) and *robo3* (E, F). Expression is seen in the apex of the fins.

G, H Double fluorescent *in situ* hybridisation of 72 hpf pectoral fins for *slit3* in green with either *robo1* (G) or *robo3* (H) in magenta.

I Schematic of the zebrafish Robo1 protein, with the position and nature of the TALEN-induced *robo1*^{sq50} lesion. Domains shown are signal peptide (pink), five immunoglobulin (Ig) motifs (red), three fibronectin type III (Fn III) motifs (yellow), a transmembrane domain (grey) and cytoplasmic domains (CC0-3; brown).

J–M Lateral Nomarski images of tail fins of 48 hpf larvae with double homozygous mutations in *robo3*^{tx209} combined with either *robo1*^{sq50} (J, L) or *robo2*^{te284} (K, M). Larvae were uninjected (J, K) or injected with 250 μM morpholino targeting *robo2* (L) or *robo1* (M). Triple-deficient larvae (L, M) show significant blistering of the fin fold compared to uninjected double-mutant controls (J, K).

Data information: Scale bars: 50 μm.

not disrupted in *slit3* mutant fins (Fig 1L). In addition, there was no obvious loss of expression of any genes previously associated with fin blisters (Appendix Fig S2). The cardia bifida mutant *miles apart* (*mil*) also displays fin blisters (Fig 3A) and corresponds to mutations in the gene encoding sphingosine-1-phosphate receptor 2 (*s1pr2*) (Kupperman *et al*, 2000). Although the hearts of *slit1a; slit3* double-mutant embryos developed normally and had normal circulation, we noted similarity between the fin defects of *s1pr2* and *slit3* mutants (Fig 3A and B). To test for synergy between the two signalling pathways, we crossed *s1pr2* and *slit3* heterozygotes, to create *s1pr2*$^{+/te273}$; *slit3*$^{+/sq49}$ trans-heterozygotes. Depending on the clutch, between 2.5 to 25% of these showed genetic interaction, presenting with tail fin blisters (Fig 3C), never seen in the respective heterozygotes (Fig 3D and E). In addition, a low frequency of *slit1a*$^{+/sq51}$; *s1pr2*$^{+/te273}$ trans-heterozygotes also showed mild blistering of the fin (Fig 3F; 5.1% (4/79) of trans-heterozygotes). Generation of trans-heterozygotes between *slit3*^{td11b} and four of the Fraser-class blistering mutants (*frem2a*^{ta90}; *hmcn1*^{tq207}; *fras1*^{te262}; *frem1a*^{tc280b}) failed to display any genetic interaction, nor did *fras1*$^{+/te262}$; *s1pr2*$^{+/te273}$ trans-heterozygotes (Appendix Fig S3A–E). $G\alpha_{13}$ is an established downstream effector of S1pr2, and reduction in both $G\alpha_{13}$ paralogues by morpholino injection results in cardia bifida and tail fin blistering in zebrafish embryos (Ye & Lin, 2013). Injection of 200 μM of the *gna13b* morpholino alone into WT embryos showed no or very mild fin morphology defects at 48 hpf, however, injection of the *gna13b* morpholino into *slit3*$^{sq49/+}$ heterozygotes produced extensive fin blistering (Fig 3G and H; Appendix Table S2). Similar enhancement of *slit3* heterozygotes was seen with *gna13a* morpholino (Appendix Table S2). Thus, reduction in S1P pathway activity at two levels, by either genetic mutation or morpholino, demonstrates interaction with the Slit-Robo pathway.

We additionally tested if *slit3* heterozygous larvae were sensitive to reduced S1pr2 signalling through use of the S1PR2 modulator, CYM-5478 (Satsu *et al*, 2013), which appears to inhibit S1pr2 in zebrafish and induces fin blisters in *s1pr2*$^{te273/+}$ embryos in a dose-dependent manner (Fig EV3A–C). One-hundred per cent of embryos derived from a *slit3*$^{+/-}$ × *slit3*$^{-/-}$ cross treated with 10–50 μM CYM-5478 displayed fin blisters, as compared to the expected 45% in untreated crosses (Fig EV3D–F). Similarly, treatment of embryos from a *slit3*$^{+/-}$ outcross with CYM-5478 invoked fin blistering in a dose-dependent manner (Fig EV3G). Genotyping indicated embryos with blisters were significantly more likely to be *slit3* heterozygotes (chi-squared; $P < 10^{-4}$; Fig EV3H). In contrast to *slit3* heterozygotes, 10 μM CYM-5478 only induces fin blisters in WT embryos at a low frequency. However, 50 μM of CYM-5478 will produce blisters in over 50% of WT embryos (Appendix Table S3). Thus, CYM-5478 acts as an S1pr2 antagonist in zebrafish and synergises with *slit3* and *s1pr2* heterozygosity, providing further evidence of Slit-Robo-S1P signalling cross-talk in maintaining fin integrity.

In situ hybridisation revealed that *s1pr2* is expressed in the mesodermally derived fin mesenchyme, while the S1P transporter, *spns2*, is expressed in a complementary manner at the AER (Fig 3I and J). This indicates that the AER cells are the likely cellular source of S1P within the fin fold. Given that Robo receptors are also found in the S1P-producing cells, while S1pr2 is expressed in Slit ligand-expressing mesenchyme, this suggests that the interaction of the pathways is sequential and not due to parallel functions. This leads to the prediction that one pathway might regulate generation of the other pathway's ligand.

Slit-Robo pathway promotes S1P signalling

We tested if S1P production is epistatic to Robo function in two ways. We attempted to increase S1P levels in *slit3* mutants, by

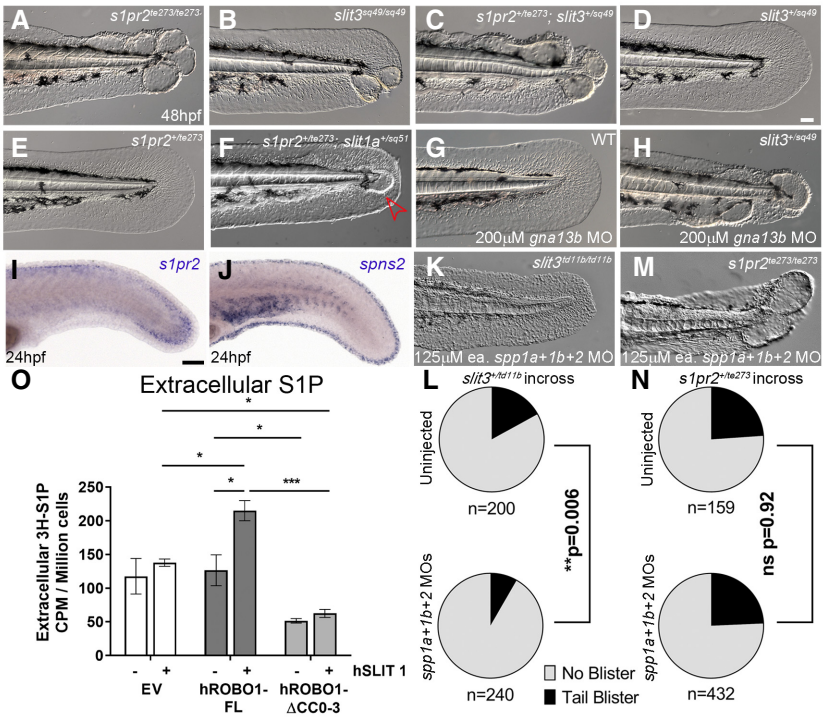

Figure 3. Sphingosine-1-phosphate signalling acts downstream of Slit-Robo signalling.

A–F Lateral Nomarski images of 48 hpf tail fins of *s1pr2*$^{te273/te273}$ (A) and *slit3*$^{sq49/sq49}$ (B) homozygous mutants, *slit3*$^{+/sq49}$ (D) and *s1pr2*$^{+/te273}$ (E) heterozygotes, *s1pr2*$^{+/te273}$; *slit3*$^{+/sq49}$ (C) and *s1pr2*$^{+/te273}$; *slit1a*$^{+/sq51}$ (F) compound heterozygotes. Blister in the compound heterozygotes highlighted with red arrowhead (F).

G, H Lateral Nomarski images of 48 hpf tail fins of WT (G) and *slit3*$^{+/sq49}$ heterozygous larvae injected with 200 μM of morpholino against *gna13b*. Seven of 191 injected AB embryos showed small blisters (3.6%), while 123 of 316 injected *slit3* heterozygous embryos showed strong blisters (39%).

I, J *In situ* hybridisation of tail fins at 24 hpf using probes detecting the reciprocal expression of *s1pr2* in the emerging mesenchyme (I) and *spns2* in the apical cells (J).

K–N Morpholino reduction in the S1P catabolic enzymes *spp1a*, *spp1b* and *spp2* rescues fin blistering of *slit3* mutants. Lateral Nomarski images of tail fins of *slit3*^{td11b} (K) and *s1pr2*^{te273} (M) mutants at 48 hpf, which were injected with 125 μM morpholinos against each of *spp1a*, *spp1b* and *spp2*. Proportion of larvae derived from *slit3*$^{+/td11b}$ (L) or *s1pr2*$^{+/te273}$ (N) heterozygous incrosses, with WT (grey) or blistered (black) fins, and injected with 125 μM of morpholinos against *spp1a*, *spp1b* and *spp2* (lower charts) or uninjected (upper charts). Significant reduction in larvae with blisters was seen between morpholino-injected and uninjected clutches from *slit3*$^{+/td11b}$ incrosses but not *s1pr2*$^{+/te273}$ incrosses (chi-squared test).

O HaCaT cells overexpressing Robo1 (dark grey bars), truncated Robo1 (light grey bars) or vector control (white bars) were metabolically labelled with ^{3}H-sphingosine. Cells were stimulated with recombinant SLIT1 (+) or unstimulated (–). Radiolabelled extracellular S1P was measured by scintillation counting and corrected for cell number. Means ± SEM shown; n = 3–4 biological replicates, *$P < 0.05$ and ***$P < 0.001$, as determined by Student's t-test.

Data information: Scale bars: 50 μm.

blocking S1P dephosphorylation. We injected three morpholinos targeting the S1P phosphatases (*spp1a*, *spp1b* and *spp2*) into embryos derived from *slit3*$^{+/td11b}$ incrosses. While 17% (n = 200) showed blistering in uninjected clutches, combined injection of *spp1a*, *spp1b* and *spp2* MOs resulted in a significantly lower frequency of blistering (8%, n = 240, $P < 0.01$; Fig 3K and L). Notably, when we genotyped all embryos with normal fins, the number of morphologically normal embryos with *slit3*$^{td11b/td11b}$ genotype was significantly higher ($P < 0.005$) in the *spp* MOs-injected group (22.5%; 18 of 80) compared to uninjected control group (5%; 4 of 80), suggesting partial rescue (Appendix Fig S4A). In parallel, we injected the *spp* MOs into offspring of *s1pr2*$^{+/te273}$ incrosses, but did not observe any rescue (Fig 3M and N) and found no increased representation of *s1pr2*^{te273} homozygotes in phenotypically normal larvae injected with the *spp* morpholinos (Appendix Fig S4B). Taken together, reducing S1P dephosphorylation cannot compensate for loss of S1pr2, but can rescue loss of Slit3. We interpret this as indicating that Slit-Robo signalling lies upstream of S1P, through regulation of S1P generation or its release.

To investigate further if activation of the Slit-Robo pathway alters production and/or release of S1P, immortalised human keratinocytes HaCaT cells were transfected with tagged versions of full-length human ROBO1 (hROBO1-FL), a dominant negative truncated hROBO1 lacking the cytoplasmic domain (hROBO1-ΔCC0-3), or an empty vector, and expression confirmed by immunoblotting (Appendix Fig S4D). After labelling of cells with ^{3}H-Sph, levels of both intracellular and extracellular S1P were measured by scintillation counting. Expression of full-length ROBO1 receptor alone had no significant effect on extracellular S1P levels, while there was a slight increase in intracellular S1P upon ROBO1 expression (Fig 3O; Appendix Fig S4C). We then stimulated these cells with recombinant hSLIT1, which resulted in a significant increase in intracellular and extracellular S1P in cells expressing the full-length hROBO1 (Fig 3O; Appendix Fig S4C). Expression of the truncated hROBO1-Δ

CC0-3 receptor significantly reduced extracellular S1P levels, compared to cells transfected with empty vector or ROBO1-FL in both stimulated and unstimulated conditions (Fig 3O). Curiously, intracellular levels of S1P were also significantly increased upon expression of hROBO1-ΔCC0-3 when rSLIT1 was supplied (Appendix Fig S4C). These results suggest that SLIT-ROBO signalling promotes synthesis and release of S1P in human keratinocytes.

S1P establishes fin mesenchyme elongation and polarity

With the S1pr2 receptor expressed on mesenchymal cells, we hypothesised that a common defect in mesenchyme behaviour and function would account for the blistering in both *s1pr2* and *slit3* mutants. We crossed both mutants to the enhancer trap line, *sqet37Et*, which labels fin mesenchyme (Lee *et al*, 2013), to visualise tissue and cell morphology and behaviour. 3D visualisation indicated large blisters form in both mutants and that the mesenchymal cells remain attached to the inner wall of the epidermis (Figs 4A–C and EV4A, and Movie EV1). Time-lapse imaging revealed that in the absence of S1pr2 or loss of both Slit1a and Slit3 ligands, distinct blisters emerge around ~ 30 hpf, continue to enlarge over the next several hours, until collapsing (Movie EV2; Fig EV4B). These movies indicated that in wild types, mesenchymal cells migrate towards the AER, but stop just before reaching it, while more proximal cells form a tiled pattern behind. These cells normally have polarised morphology with a proximally positioned cell body and nucleus. They typically have one to three long directional protrusions orientated towards the distal fin tip (Figs 4A and EV4B). Such protrusions are particularly prevalent for the tier of mesenchyme nearest the apex (Tier 1 cells). The elongation increases over time as the cells migrate distally, such that in wild-type embryos, mesenchymal cells reduce their circularity, increase eccentricity and elongate as they approach the periphery between 24 and 40 hpf. In both mutants, mesenchymal cells maintain their circularity throughout, fail to increase either their eccentricity or their length (Figs 4D and I, and EV4C–E; Movies EV2–EV4). All geometric features analysed were statistically different between both mutants and wild types at the 95% confidence interval (Fig EV4F–H).

High-resolution tracking of WT mesenchyme during migration indicated that these cells exhibited active filopodia directed towards the outer fin edge and directional movement away from their proximal origin (Fig 4G and J; Movie EV4). In contrast, mesenchyme positioned in the developing blisters of *slit3* or the *s1pr2* mutants showed a discoidal morphology with multiple small, active yet short-lived protrusions. These protrusions rapidly retracted and occurred in all directions around their periphery, implying impaired polarity (Fig 4H and I; Movie EV4). Indeed, migratory tracks of such cells in mutant embryos exhibited no directional preference and an overall reduced displacement towards the AER (Figs 4K and L, and EV4I and J).

We determined the orientation of the cells towards the AER by measuring the angle from the nucleus through the microtubule organising centre (MTOC; marked by γ-tubulin) to the nearest point of the AER (Fig 4M). In WT embryos, cells closest to the AER (Tier 1 cells) were the most polarised in the direction of migration, with angle to AER almost always close to 180°, with cells progressively further from the AER (Tier 2 and Tier 3 cells), less orientated towards the periphery (Fig 4N and O). In contrast, MTOCs in all mesenchyme of both *slit3* and *s1pr2* mutants were orientated far more randomly with respect to the nucleus and the nearest point on the AER (Fig 4N and O), and appeared to lack polarity.

We conclude that while mesenchyme in both *slit3* and *s1pr2* mutants adhere to the inner surface of the fin epithelium, they fail to polarise or generate productive filopodia, and do not correctly migrate towards the AER.

S1P is required for stress fibres in mesenchyme

The fin malformations developed below the basement membrane and initiated around the mesenchyme. Thus, we hypothesised that the altered mesenchymal cell morphology and blistering in both mutants result from loss of cytoskeleton organisation or cellular adhesive mechanisms, such as focal adhesions and stress fibres. Indeed, S1PR2 signalling is well known to induce stress fibre formation and inhibit cell migration via $G\alpha_{12/13}$ activation of PDZ-RhoGEFs (Yamamura *et al*, 2000). Furthermore, either suppression of $G\alpha_{13}$ expression or injection of a dominant negative form of Arfgef11 (a PDZ-RhoGEF) results in tail blisters (Ye & Lin, 2013). To visualise cellular focal adhesions and stress fibres, we performed immunofluorescent staining for phospho-focal adhesion kinase (pFAK) and phospho-non-muscle myosin II (pNM-myosin II) respectively. WT fin mesenchyme had strong staining of both pFAK and pNM-myosin II localised to the distal protrusions of the most apical cells (Fig 5A, A' and B, B'). Strikingly, there was a gradient of signal across the fin with high signal apically (in Tier 1 cells) and significantly much less signal in proximal mesenchyme (in Tier 2 and 3 cells as designated in Fig EV5A and B). Signals in Tier 1 cells were concentrated in the apically orientated cell processes. Both *s1pr2* and *slit3* mutant mesenchyme had significantly reduced pFAK or pNM-myosin II signal in Tier 1 cells, and no gradient of immunofluorescence across the fin. The levels of these markers were low irrespective of location in the fin fold (Figs 5A, A' and B, B', and EV5C and D). Furthermore, any signal observed was not orientated apically, but occurred around the cell body. We conclude that focal adhesions and stress fibres are apically localised in WT fins and are reduced in both mutants.

Fibronectin1a (Fn1a) (Trinh & Stainier, 2004), in concert with Spns2 (Hisano *et al*, 2013), S1pr2 (Matsui *et al*, 2007) and $G\alpha_{13}$ (Ye *et al*, 2015), is required for the migration of myocardial precursors. While the fins of most *fn1a* mutants appear normal, the interaction of *fn1a* with *gα13* in cardiac migration suggests that they may interact during fin morphogenesis. Low doses of *fn1a* or *gna13b* MOs alone yielded no or rare fin blisters, respectively, but following combined injection, 74% of larvae had distal fin blisters reminiscent of those in *slit3* and *s1pr2* mutants (Fig 5C and F–H). Similarly, injection of non-phenotypic doses of *gna13a* and *gna13b* MO into *fn1a* mutants or heterozygotes significantly increased the proportion of larvae with blisters, compared to WT injected with these MOs (Fig 5H). Given that we have linked Slit-Robo signalling with the S1P–*gα13* pathway, we would expect that *slit3* mutation might interact with partial loss of Fn1a. Indeed, injection of low doses of *fn1a* MO into *slit3* heterozygotes realised about 18% of larvae with fin blisters (Fig 5C–E). Immunostaining for fibronectin indicates it is localised to the fin fold interstitium, and that fibronectin protein remains in the fin dermis of both *slit3* and *s1pr2* mutants (Fig EV5E–G).

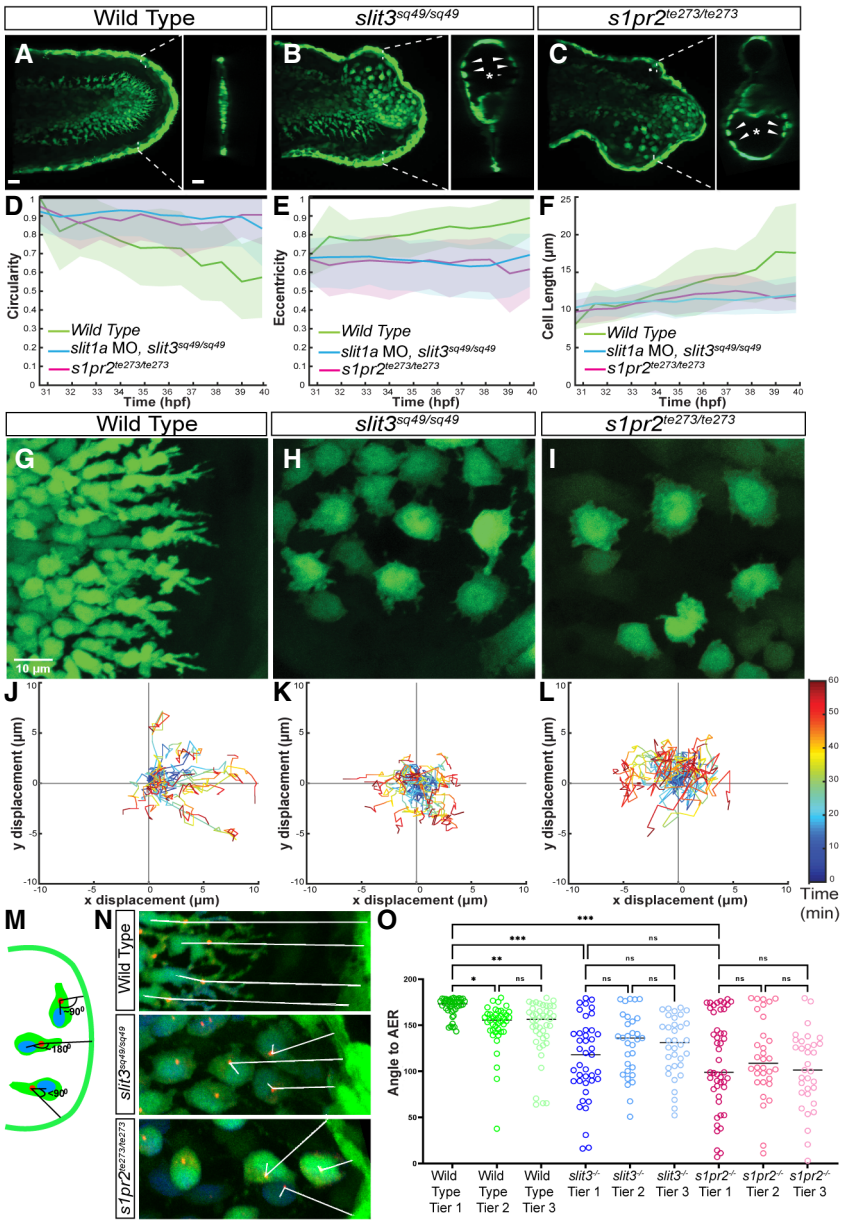

Figure 4. Mesenchymal cells of both mutants show abnormal morphology and loss of polarity.

A–C Confocal projections of the 40 hpf tails of WT (A), *slit3*^{sq49} (B) and *s1pr2*^{te273} (C), crossed to *sqet37Et*, labelling the fin mesenchyme in eGFP. Insets show transverse orthogonal slice at the indicated location. The mutant mesenchymal cells are attached to the inner wall of the blister as indicated by arrowheads. Scale bar indicates 20 μm.

D–F Changes in mesenchyme circularity (D), eccentricity and length (E) as the cell migrates away from the paraxial mesoderm, between 30 and 40 hpf. Three embryos were tracked for each condition, and 33 cells of WT, 33 cells of *slit3*^{sq49} and 35 cells of *s1pr2*^{te273} were analysed.

G–I WT cells (G) close to the apex have an elongated and polarised appearance while both mutants are unpolarised and have a disc-like appearance (H, I, centre and right panels).

J–L Tracks of cells from WT (J) *slit3*$^{-/-}$ (K) and *s1pr2*$^{-/-}$ (L) embryos over 60 min duration. Mutants display a lack of directionality and reduced displacement over a short range. Tracks are normalised to a common start point, 23 cells of WT, 22 cells of *slit3*^{sq49} and 21 cells of *s1pr2*^{te273} from three to four embryos were tracked.

M–O Schematic describing of the measurement of a cell's approach angle to the nearest point on the AER (M). Merged, immunofluorescent images of WT (top), *slit3*^{sq49} (centre) and *s1pr2*^{te273} (below) mesenchymal cells in *sqet37Et* background stained for EGFP (green), gamma tubulin (red) and DAPI (blue). White lines run from the centre of nucleus to the nearest point on the AER, through the MTOC (N). Graph depicting the approach angles to AER of leading (Tier 1), following (Tier 2) and trailing (Tier 3) cells of WT, *slit3*^{sq49} and *s1pr2*^{te273} embryos (O). A minimum of 30 cells were measured for each tier of each genotype. *$P < 0.05$; **$P < 0.005$; ***$P < 0.001$; ANOVA with Fisher's post-test.

Data information: Scale Bars: 50 μm (A), 10 μm (G).

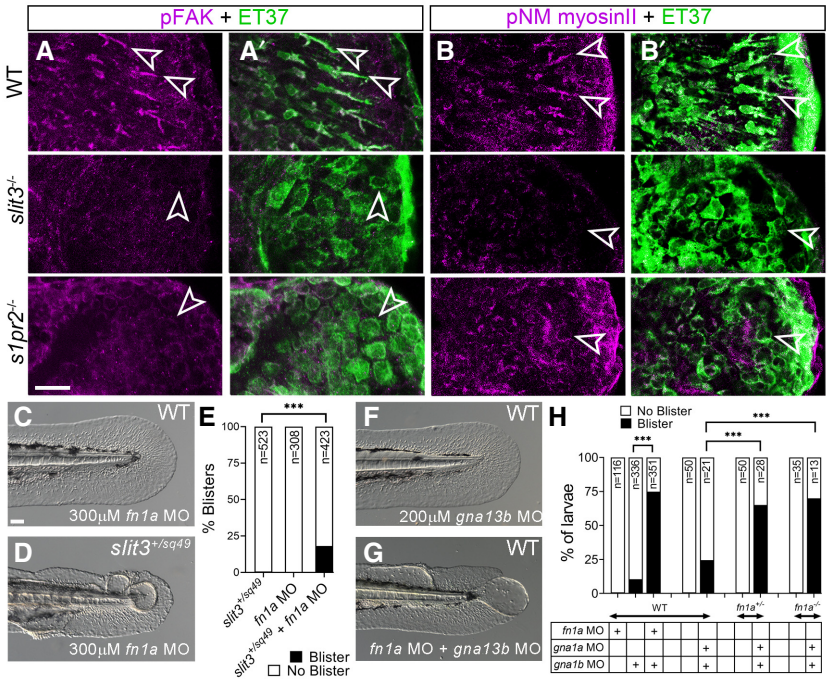

Figure 5. Both *slit3* and *s1pr2* mutants show loss of focal adhesion markers and sensitivity to fibronectin levels.

A, B Immunofluorescent staining of 48 hpf tail fins in WT *sqet37Et* (Top row), *slit3*$^{sq49/sq49}$; *sqet37Et* (middle row) and *s1pr2*$^{te273/te273}$; *sqet37Et* (bottom row) transgenic larvae, stained for phospho-FAK (magenta; A, A'), phospho-non muscle myosin II (magenta; B, B') and eGFP (green; A', B'). Mutant mesenchymal cells show significantly reduced p-FAK and p-NM myosin II (magenta; A, B) signals in *slit3* and *s1pr2* homozygous mutants compared to the WT fin mesenchyme. Arrowheads indicate fin mesenchymal cells.

C–E Lateral Nomarski images of 48 hpf larval fins which are WT (C) or *slit3*$^{+/sq49}$ heterozygotes (D) and are injected with 300 μM *fn1a* morpholino. Blisters are observed only when there is reduced Fn1a in *slit3* heterozygotes (quantified in E).

F, G Lateral Nomarski images of 48 hpf WT larval fins injected with 200 μM *gna13b* alone (F) or with 300 μM *fn1a* morpholino (G).

H Quantification of the proportion of larvae with fin blisters when low amounts of *gna13* morpholinos (125 μM each *gna13a* and *gna13b* MO combined or 200 μm *gna13b* MO alone) are injected into WT, *fn1a* morphants (300 μM MO), *fn1a*$^{+/-}$ heterozygotes and *fn1a*$^{-/-}$ mutants. Loss of a single or both copies of *fn1a* exacerbates reduced *gna13* levels, as does knockdown of *fn1a*.

Data information: ***$P < 0.001$, Chi-squared tests used in (E) and (H). Scale bar (A, B): 20 μm; (C–G): 50 μm.

We thus propose that S1P is acting through S1pr2 and Gα_{13} to establish mesenchyme adhesion to Fn in the interstitial ECM. These mesenchymal cells indeed specifically express integrin receptors for fibronectin, Itgb3b and Itgav, which are known to promote fibroblast contractility on Fn substrates (Fiore *et al*, 2018; Fig EV5H and I). However, attempts to ablate these proteins by morpholino yielded moderate gastrulation and axis defects and CRISPR mutants had no phenotype, suggesting compensation.

Directed mesenchyme migration by a self-generated signalling gradient interacting with the fin boundary

Combining our above observations, we hypothesise that the S1P-activated adhesion of the mesenchymal cells imparts tension on fibronectin in the interstitial ECM, retaining the two epidermal sheets of the fin fold in close proximity, while also promoting mesenchyme polarity and migration (Fig 6A).

Why this reciprocal signalling between mesenchyme and apical ridge cells has been established in the fin is not clear. As S1P is released from a discrete source at the apex, it likely forms a gradient along the distal–proximal axis of the fin fold, and hence a gradient of adhesiveness, as seen by pFAK and pNM-myosin II staining. Proximity of Slit expressing mesenchyme to the apical domain might alter the level of S1P release, which would act to sharpen the adhesion gradient of the mesenchyme as it approaches the fin fold apex.

To test whether this idea is plausible to direct cell migration, we constructed a simple model of the interactions between the migrating cells, which secrete Slit, with a return gradient of S1P (Methods). Our simulation results suggest that such a mechanism may allow the cell to direct its own migration by interacting with the boundary to adjust its velocity as they migrate (Fig 6B–C). The cell is brought to a final position within the tissue environment when the adhesion strength prohibits further migration. This mechanism enables fine tuning of the adhesion experienced by the cell as it migrates through the fin fold; in essence, cells can regulate the haptotactic field they encounter during migration to the apex and alter tissue shape as cells approach their destination.

Discussion

It has been established that there is a distal–proximal gradient of cell–cell adhesion in the forming limb bud, critical for correct morphogenesis (Wada, 2011). Whether cell–matrix adhesion also

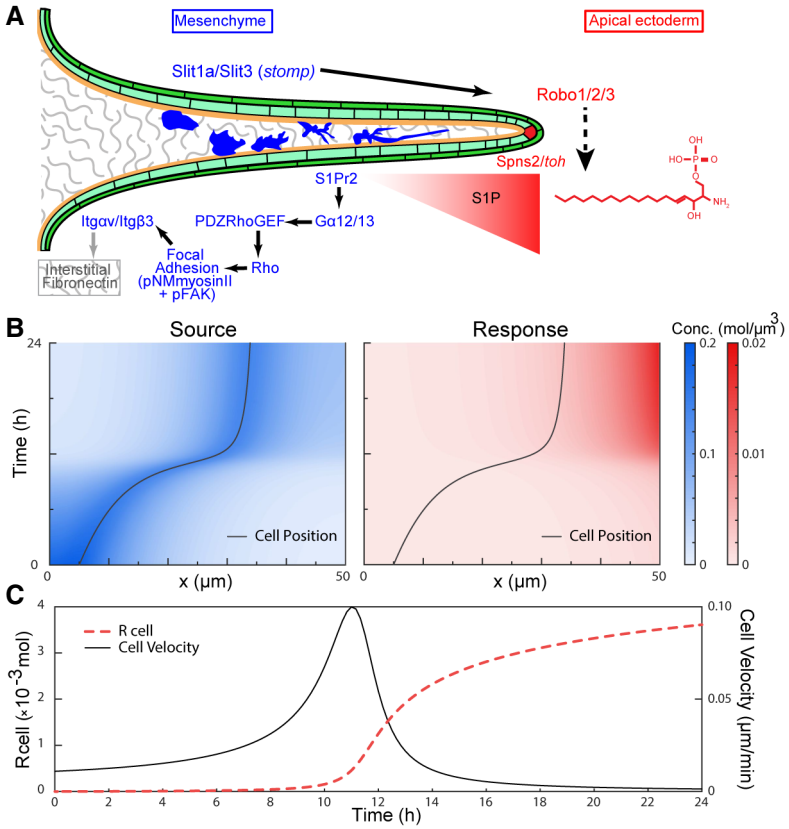

Figure 6. Reciprocal signalling of Slit-Robo and S1P creates an adhesion gradient that modulates cell migration.

A Model of Slit-Robo and S1P signalling deployment in the fin fold (light and dark green), with apical ridge cell in red and mesenchymal cells in blue invading the fin. Fibronectin of the interstitial ECM is in grey stipples. Components found in or generated by the mesenchymal cells are listed in blue, while those of the apical ridge cells are in red. The gradient of S1P (red) is shown as a triangle and the pathway activated by S1PR2 in mesenchymal cells is shown in blue, culminating in adhesion to interstitial fibronectin (grey). Robo signalling promotes production and or release of S1P (dashed arrow).

B, C Computer simulation of a single mesenchymal cell migrating towards the apical ridge ($x = 50$ μm) under reciprocal signalling. The cell emits a source signal, S, which induces the production of a response signal, R, from the apical ridge (B). The resulting cell velocity depends on the amount of R present at the cell position, R cell, with moderate levels of R cell resulting in the highest cell migration rates (C).

shows a gradient is not known. Additionally, limb bud mesenchyme polarity and migration are defined by AER-derived signals such as Wnt5a, and that cell proximal–distal elongation drives limb morphogenesis (Gros *et al*, 2010; Wyngaarden *et al*, 2010). It has been proposed that the distal–proximal gradient of adhesion cooperates with orientated cellular behaviour for morphogenesis (Wada, 2011). Our work uncovers an unexpected role for the Slit-Robo pathway in the morphogenesis of the medial and paired fins of zebrafish, considered to be the evolutionary precursors of tetrapod limbs. In *slit3* mutants, fin mesenchyme has defects in polarity, stress fibre formation, fibronectin adhesion and migration leading to disrupted fin morphology. The tissue, cellular and molecular defects of *slit3* mutants are replicated in the fins of the *s1pr2* mutant, and we see synergy between the Slit-Robo and S1P signalling pathways by combined genetic and/or pharmacological disruption. Localisation of the receptors of the two pathways, as well as genetic epistasis analysis, supported a model of Robo signalling promoting generation or release of S1P from the fin AER. This was corroborated by *in vitro* S1P biochemical assays which also suggested this regulation occurs in mammalian cells. In turn, S1P is received by the immigrating mesenchymal cells, where the relevant receptor, S1pr2, is expressed. Activation of S1PR2 is described to induce stress fibres and focal adhesions via Rho (Wang *et al*, 1997), and we observe loss of markers of both these adhesive structures in both *slit3* and *s1pr2* mutants. Furthermore, we have seen that partial loss of components of the Slit-Robo or S1P pathways render larval fins sensitive to reduced levels of fibronectin. We hypothesise that the mesenchymal cells bind to interstitial fibronectin via their activated focal adhesion complexes and S1P activation of myosin in the stress fibres both promotes initial directional migration and also provides tension on the interstitial matrix of the most distal fin fold. It is plausible to consider that this tension retains the two epidermal sheets of the fin fold in close proximity. These results are summarised in Fig 6A.

Missense mutations in *S1PR2* have been found in three families with autosomal recessive hearing impairment (Santos-Cortez *et al*, 2016; Hofrichter *et al*, 2018). Intriguingly, for one of these families, all individuals with hearing impairment also had distal limb anomalies. As they were not seen in the other families or the *S1pr2* mouse mutants, a role for S1PR2 in limb development was excluded;

however, no other mutations were identified that may account for these limb malformations, and the cause in this family remains unidentified. Given our identification of defects in mesenchyme morphology in *s1pr2* mutant fins, it may be worth revisiting a partially redundant role for S1PR2 signalling in human limb development.

How Robo signalling promotes secretion of S1P is unclear. We found *spns2* mRNA expressed at normal levels in *slit3* mutant fins and *slit3* is unlikely to act via *sphk2* transcriptional regulation, as maternal *sphk2* alone is sufficient for normal fin formation (Mendelson *et al*, 2015). Robo receptors do not have enzymatic activity and, following binding by Slits, recruit activators to their intracellular domains. These include a number of actin cytoskeleton regulators including Slit-Robo GAPs (SrGAPs), Sos and Pak (Blockus & Chedotal, 2016). We see co-expression of *srgap1a* and *srgap2* with the *robo* genes in the apical fin fold. However, combined morpholino knockdown of these *srgap* genes did not elicit a blister phenotype. It has been shown that Slit induces recruitment of Sos to the Robo receptor through promoting endocytosis of the ligand–receptor complex, and that Sos can access Robo only present in endosomes (Chance & Bashaw, 2015). In parallel, Shen *et al* have demonstrated that SPHK1 and SPHK2 both bind strongly to endocytic structures (Shen *et al*, 2014). However, our cell culture experiments, using overexpression of ROBO1 receptor and recombinant SLIT1, failed to show clear alteration of the sub-cellular localisation of SPHK2 or SPNS2.

Despite being mostly known for its role in axon guidance and neuron cell migration in both vertebrates and invertebrates (Kidd *et al*, 1999; Jen *et al*, 2004), a role for Slit-Robo signalling in morphogenesis is not novel. A patient with a translocation mutation affecting *ROBO2* has been described to have clinodactyly and syndactyly in addition to kidney and urinary tract defects (Lu *et al*, 2007), while a dominant *de novo* missense mutation in *SLIT2* was found in a patient with myopia and dermal connective tissue defects (Liu *et al*, 2018). Perturbation of Slit-Robo signalling leads to cardiac malformation in human, mouse, zebrafish and *Drosophila* (MacMullin & Jacobs, 2006; Fish *et al*, 2011; Mommersteeg *et al*, 2015; Kruszka *et al*, 2017). In the latter two species, Slit-Robo signalling is essential for migration of cardiac precursors to the midline (Santiago-Martinez *et al*, 2008; Fish *et al*, 2011). In particular, medially migrating endocardial cells in zebrafish *slit2* morphants show dynamic filopodia but lack directionality, reminiscent of the mesenchyme of the fins in *slit3* and *s1pr2* mutants. Thus, both S1P and Slit-Robo signalling have been associated with cardiac precursor migration defects. While we link the two pathways in fin morphogenesis, curiously the *slit3*, *slit1a* or *robo1* mutants did not show an overt defect in heart morphogenesis, despite all three showing distinct similarities with fin blisters in *s1pr2* mutants (*miles apart*). It is possible that sub-functionalisation of *slit* genes has led to *slit2* functioning in the cardiac field while *slit1a* and *slit3* are important for fin morphology.

Examples of interaction of the Slit-Robo pathway with other cell signalling systems are limited (Blockus & Chedotal, 2016). Our work identifies a novel relay signalling system between the AER and the immigrating mesenchyme which is essential for cell–ECM adhesion, polarity and fin morphogenesis. This will refine biophysical models of how limb and fin outgrowth are constrained into precise morphologies.

Materials and Methods

Zebrafish strains and husbandry

Zebrafish were maintained in IMCB fish facility under standard conditions at 28°C on a 14 h light–10 h dark cycle. Embryos were obtained through natural matings, raised at 28°C in E3 medium (5 mM NaCl, 0.17 mM KCl, 0.33 mM $CaCl_2$ and 0.33 mM $MgSO_4$) and staged according to Kimmel *et al* (1995). The following lines were used: AB wild type, *sto*^{td11b}, *frem2a*^{ta90} (=*blasen*, *bla*), *hmcn1l*^{tq207} (=*nagel*, *nel*), *fras1*^{te262} (=*pinfin*, *pif*), *frem1a*^{tc280b} (=*rafels*, *rfl*) (all described previously in van Eeden *et al* (1996)), *s1pr2*^{te273} (=*miles apart*, *mil*) (Kupperman *et al*, 2000), *robo2*^{te284} (=*astray*, *ast*) (Fricke *et al*, 2001), *robo3*^{tx209} (=*twitch twice*, *twi*) (Burgess *et al*, 2009) and the *sqet37Et* (ET37) enhancer trap line (Lee *et al*, 2013) in *slit3*^{sq49} and *s1pr2*^{te273} backgrounds. *slit3*^{sq49}, *robo1*^{sq50} and *slit1a*^{sq51} mutants were generated as described below. The *slit3*^{sq49} mutation is a frame-shifting indel, c.1141_1147delinsATG; p.His238MetfsTer20. The *slit1a*^{sq51} mutation is also a frame-shifting indel, c.269_274delinsCCGACGCGCCGCGC; p.Ile90ThrfsTer15. The *robo1*^{sq50} mutation is a 13bp deletion leading to a frame-shift c.1396_1408del; p.Gln466GlufsTer78. All experiments were conducted under A*STAR BRC IACUC oversight (IACUC number 140924) and NTU IACUC oversight (A18002).

Genetic mapping

For genetic mapping, *sto*^{td11b} was crossed onto the WIK background and mutant and sibling offspring were each pooled for bulk segregant analysis following Geisler (2002). This led to an assignment to linkage group 14. Fine single-sequence linkage polymorphism mapping was then conducted on 430 single-mutant embryos, placing the *sto* locus between z6847 and z22128. SNP markers were developed to refine the interval to a 1.1 Mb interval. The coding regions and intron–exon boundaries for the 11 genes in that interval were sequenced and a mutation in *sto* larvae was identified in Intron 9 of the *slit3* gene.

TALEN and CRISPR mutagenesis

Mutagenesis of *slit3* or *robo1* was performed by design, assembly and injection of TALEN constructs, which were made to target sites in exon 8 of each gene. For the *slit3* gene, the dimeric TALENs bound the following sites (5′-3′) in exon 8; Left: CACACAGTGCATGGCC; Right: CAGGGACATTGAGACC. For the *robo1* gene, the TALENs bound the following sites (5′-3′) in exon 8, Left: CCACACATGATTCCCG; Right: CTGCAGGGCTCCAGTG. Repeat variable di-residue (RVD) recognition modules for the above target binding sites were fused to the left or right monomer of the heterodimeric variant of FokI nuclease using the Golden Gate system as per Dahlem *et al* (2012). Mutagenesis of *slit1a* was performed using the CRISPR-Cas9 system with the guide RNA targeting the exon 3 sequence 5′-GGAGAACCAGATTGTAACGG-3′. A PCR product containing a T7 promoter directly upstream of the sgRNA was generated using overlapping primers as per Bassett *et al* (2013). TALEN and Cas9 RNAs were generated from plasmids linearised with NotI and synthesised with the mMessage Machine SP6 kit (Invitrogen) according to instructions. The *slit1a* sgRNA was synthesised from

purified PCR product using the MEGAshortscript™ T7 kit from Invitrogen as per manufacturer's instructions.

Following injection of TALEN RNAs or *slit1a* CRISPR sgRNA with Cas9 RNA into wild-type embryos, a selection of larvae was sequenced to confirm efficient mutagenesis. The remaining larvae were raised to adulthood, incrossed and selected larvae sequenced for identifying founder adults carrying mutations.

Morpholinos and inhibitors

Morpholinos (MOs) used and their sequences (5′-3′) were as follows:

slit3 ATG*:* CCCCCAATACTTTACCCACCGCATC; *robo1* ATG: AT CCAATTATTCTCCCCGTCATCGT; *robo2* ATG: GTAAAAGGTGTGT TAAAGGACCCAT; *spp1a* ATG: ACCCCGCTTTTATCCCGCCTGCC AT; *spp1b* ATG: ATCTGTGGAGCACGTCGCTTGCCAT; *spp2* ATG: TCAGGTACGTGATGATTCTCCACAT; *fn1a* ATG: TTTTTTCACAG GTGCGATTGAACAC; *gna13a* ATG: AAATCCGCCATCTTTGTAGTA GCGA; *gna13b* ATG: AGGAAATACGCCATCTTTGTGCAAC.

All MOs were obtained from GeneTools and dissolved to a stock concentration of 1 mM in distilled water. For injection, stock MOs were diluted in 1X Danieau's solution: 5 mM HEPES (pH 7.6), 58 mM NaCl, 700 μM KCl, 400 μM $MgSO_4.7H_2O$ and 600 μM Ca $(NO_3)_2$ with 0.5% phenol red and injected (125–500 μM) individually or in combination into one-cell-stage embryos.

S1pr2 selective modulatory agent, CYM-5478 (Aobious), was dissolved in DMSO as 25 mM stock solution and added to embryos from 3 to 48 hpf at final concentration of 10–50 μM, and then scored for fin fold abnormalities.

Microscopy and sectioning

Bright-field and Nomarski images were taken on a Zeiss AxioImager M2, while fluorescent images were taken on a Zeiss LSM700 confocal. A Zeiss LSM800 confocal was used for all time-lapse confocal movies. Live embryos were mounted in 3% methyl cellulose for Nomarski images of the tail. For time-lapse movies, embryos were anaesthetised in 0.02% tricaine buffered to pH7.0 and mounted in 0.7% low melting point agarose in glass-bottomed imaging dishes. Embryos were then overlaid with 0.5× E2 medium (7.5 mM NaCl, 0.25 mM KCl, 0.5 mM $MgSO_4$, 75 μM KH_2PO_4, 25 μM Na_2HPO_4, 0.5 mM $CaCl_2$ and 0.35 mM $NaHCO_3$) containing 0.02% tricaine (buffered to pH 7.0), and the agarose around the tail was excavated to permit free movement during growth.

For coronal sections, cryosectioning of embryos was performed using a Leica CM1900 cryostat and the 16 μm sections were then stained by haematoxylin & eosin.

Image processing, cell shape analysis, tracking and statistics

All microscopy images were processed using Zen 3.1 software (Zeiss), Fiji (ImageJ, ver. 1.52p) or Imaris (Bitplane).

Images of developing zebrafish fins were aligned in 3D using a custom MATLAB code, and image segmentation was done using the surfaces function in Imaris 9.2.1. Quantification of the segmented data was done using the functions regionprops and regionprops3 in MATLAB.

Circularity, eccentricity and length of the cells, as they migrate away from the paraxial mesoderm, were measured on time-lapses (20× magnification), obtained between 30 and 40 hpf. The shortest Euclidean distance between the cell centroid and the paraxial mesoderm is measured and binned at 10 μm intervals. Within each distance interval, the mean and standard deviation of the circularity, eccentricity and length measures were calculated for cells of each condition. Three embryos were tracked for each condition, 33 cells for WT, 33 cells for *slit3*^{sq49} and 35 cells for *s1pr2*^{te273}.

Cell circularity specifies the roundness of the object and is defined as $\frac{4\pi\,Area}{(Perimeter)^2}$, such that a perfect circle has a circularity value of 1. Cell eccentricity gives the elongation of the object and is defined as $\sqrt{1-\frac{(Minor\ Axis\ Length)^2}{(Major\ Axis\ Length)^2}}$ so that an ellipse with an eccentricity of 0 is a circle. The length of each cell is given by its major axis length.

To compare the physical changes in the cell over time in the two mutants to those in the wild type, we fitted a line to each cell track and then statistically analysed the resulting slopes. Cells from each condition were aggregated for the analysis, giving $N = 33$, 33 and 35 cells for the WT, *slit3*$^{-/-}$ and *s1pr2*$^{-/-}$ conditions respectively. The estimation plots and statistical analysis were generated with the statistical software DABEST (Ho *et al*, 2019).

Cell tracking was performed on time-lapse images (40× magnification), obtained between 36 and 43 hpf. The images were drift corrected with Imaris (Bitplane) to negate movement due to tissue growth, and further manually tracked using Fiji. The XY coordinates obtained were plotted using MATLAB.

A cell's approach angle to AER was measured using the angle tool function of Fiji/ImageJ, with nucleus and MTOC as anchor points. Mesenchymal cells closest to the AER (most distally positioned) are considered Tier 1 cells. Cells positioned immediately behind Tier 1 cells are designated as Tier 2 cells. Tier 3 cells are positioned behind (proximal) the Tier 2.

The intensities of pFAK and pNM-myosin II were measured on embryos co-immunostained for eGFP. The leading ends of Tier1, Tier2 and Tier3 cells were marked on the eGFP channel (ET37 signal), using the multi-point tool of Fiji/ImageJ. These marked ROIs were used to measure signal intensities on the pFAK or p pNM-myosin II stainings seen in red channel.

Statistics were performed using Graphpad Prism using *t*-test, chi-squared tests or ANOVA with Tukey's or Fisher's post-tests. Graphs depict mean plus standard deviations unless otherwise stated.

PCR, *in situ* hybridisation and antibody staining

Sequences for generating probes were amplified from cDNA by PCR using GoTaq DNA Polymerase (Promega) on a BioRad T100 Thermal cycler. Amplicons were purified using a Qiagen PCR purification kit, and then cloned into pGEMT-Easy (Promega). For the following probes, plasmids were linearised with *SacII* (NEB): *slit2*, *robo1*, *robo2*, *robo3*, *s1pr2* and *spns2*. The *slit1a and slit1b* plasmids were linearised with *ApaI*, while *slit3* probe plasmid was linearised with *MfeI*. For all RNA *in situ* probes, the SP6 DIG labelling kit (Roche) was used for transcription, except for *slit3* probe, which used either the T7 DIG or T7 Fluorescein labelling kits (Roche). Whole-mount *in situ* hybridisation on embryos was performed as per Thisse and Thisse (2008), and developed using NBT/BCIP (Roche) and cleared in glycerol for imaging. Double fluorescent *in situ* hybridisation was performed using fluorescein-

labelled *slit3* probe and DIG-labelled *robo1* or *robo3* probes according to Brend and Holley (2009).

For immunofluorescent antibody stainings, embryos were fixed with 4% PFA for 2 h room temperature, except for anti-pNM-myosin II and anti-pFAK stainings, which used 95% MeOH with 5% glacial acetic acid at −20°C for 4 h. Embryos were permeabilised in Acetone for 7 min at −20°C, washed in PBS with 0.5% Triton, blocked for 2 h in Block solution (PBS Triton with 0.5% goat serum and 0.1% dimethyl sulfoxide) and then incubated in Block with primary antibody. After extensive washing in PBS Triton, embryos were incubated with secondary antibodies overnight in Block solution, and then rewashed in PBS Triton before clearing in glycerol for imaging. Primary antibodies, sources and dilutions used were as follows: mouse anti-TP63 (=ΔNp63; Clone 4A4; Biocare, Cat# CM163; RRID:AB_10582499; 1:500), rabbit anti-laminin (Sigma, #L9393; RRID:AB_477163; 1:200), rabbit anti-zebrafish Fras1 ((Carney *et al*, 2010), 1:50), rabbit anti-eGFP (Torrey Pines Biolabs, #TP401; RRID: AB_10013661; 1:1,000), rabbit anti-fibronectin (F3648, Sigma-Aldrich; RRID:AB_476976; 1:200), rabbit anti-phospho-FAK pY861 (#44-626G; Thermo Fisher Scientific; RRID:AB_2533703; 1:250), rabbit anti-phospho-myosin light chain II (S19; pNM-myosin II) (#3671; Cell Signalling Technology; RRID:AB_330248; 1:250) and rabbit polyclonal anti-gamma tubulin (GTX113286, GeneTex; RRID: AB_1952442; 1:250). Secondary antibodies were sourced from Invitrogen and used at 1:400: Alexa 488-conjugated donkey anti-rabbit IgG (Cat# A-21206, RRID:AB_2535792), Alexa 546-conjugated donkey anti-mouse IgG (Cat# A10036, RRID:AB_2534012) and Alexa 647-conjugated donkey anti-rabbit IgG (Cat# A-31573, RRID: AB_2536183). Counterstaining of nucleic was performed using 1 μg/ml DAPI (Thermo Fisher Scientific).

Generation of Robo1 expression vectors

Human Robo1 full-length (FL) cDNA (GenBank accession number: NM_133631.3) was cloned with a C-terminal 3xHA tag into pcDNA3 from a hRobo1 ORF clone by PCR to generate hRobo1-FL-3xHA(C)/pcDNA3. The dominant negative truncated hRobo1 construct, hRobo1$^{\Delta CC0\text{-}3}$-3xHA(C)/pcDNA3, which included the first 920 amino acids (excluding the CC0-3 cytoplasmic domains) were PCR amplified from the hRobo1-FL-3xHA(C)/pcDNA3 plasmid.

Cell culture and S1P production assay

HaCaT cells were cultured in Dulbecco's modified Eagle's medium (DMEM) containing 10% foetal bovine serum and 100 units/ml penicillin and 100 μg/ml streptomycin in a 5% CO_2 humidified incubator. The rate of S1P formation in intact cells was determined as an *in situ* assay of SphK activity as described previously (Zhu *et al*, 2017). Briefly, HaCaT cells were transfected with pcDNA3, hRobo1-FL-3xHA(C)/pcDNA3 or hRobo1$^{\Delta CC0\text{-}3}$-3xHA(C)/pcDNA3 using Lipofectamine2000 (Thermo Fisher Scientific) and incubated for 24 h and then sub-cultured into 12-well culture dishes and allowed to bed down overnight. The cells were then labelled with 0.25 μCi of [^{3}H]-sphingosine (Perkin-Elmer) in serum-free DMEM with 0.1% fatty acid–free BSA with and without the addition of 10 μg/ml recombinant Slit1 protein. After 30 min incubation at 37°C in a humidified atmosphere of 5% CO_2, the conditioned medium was removed and the cells washed and scraped into cold PBS. [^{3}H]-S1P formed during the 30 min incubation was then extracted from both the conditioned medium and cell pellets via a modified Bligh–Dyer extraction. Briefly, 300 μl of acidified methanol (100:1, methanol: concentrated HCl) was added to the cell pellets and then sonicated for 30 s in an ice bath. To each cell sample, 300 μl of 2 M KCl, 300 μl of chloroform and 30 μl of 3 M NaOH were then added. After vigorous mixing and centrifugation at 13,000 *g* (5 min), a phase separation enabled separation of S1P in the upper aqueous methanol phase from sphingosine in the lower chloroform phase. The [^{3}H]-S1P in the upper aqueous methanol phase was then analysed by scintillation counting (Microbeta, Perkin Elmer). Extracellular [^{3}H]-S1P in the conditioned medium (500 μl) was analysed in the same manner with the addition of 500 μl of methanol, 500 μl of chloroform and 50 μl of 3 M NaOH. All analyses were performed in triplicate and corrected for total cell number.

Mathematical model

We model the reciprocal signalling for a single cell, with position x_{cell}, migrating on a static one-dimensional spatial domain bounded by the notochord ($x = 0$) and the apical ridge ($x = L$). Let $S(x, t)$ denote the concentration of a "Signal" molecule secreted by the migrating cell, corresponding to the Slit. Let $R(x, t)$ denote the concentration of a "Response" signal that originates from the apical ridge, corresponding to S1P.

The concentrations of the source S and the response R are described by:

$$\frac{\partial S}{\partial t} = D_S \nabla^2 S - \mu_S + J_S \cdot \delta(x - x_{cell})$$

$$\left.\frac{\partial S}{\partial x}\right|_{x=0} = 0 \quad for\ t > 0$$

$$\left.\frac{\partial S}{\partial x}\right|_{x=L} = 0 \quad for\ t > 0$$

$$\frac{\partial R}{\partial t} = D_R \nabla^2 R - \mu_R$$

$$\left.\frac{\partial R}{\partial x}\right|_{x=0} = 0 \quad for\ t > 0$$

$$D_R \left.\frac{\partial R}{\partial x}\right|_{x=L} = -j_R \cdot f(S(L))$$

S is produced with rate J_S at the position of the cell x_{cell}, degrades with rate {$_S$ and diffuses with a diffusion coefficient D_S. It has zero flux at the left and right boundaries. R is produced as a function of the amount of S on the right boundary, scaled by a production factor, $-j_R$, diffuses with diffusion coefficient D_R and degrades with rate μ_R. It also has a zero-flux boundary condition on the left. L = 50 μm; x_{cell} ($t = 0$) = 5 μm; D_S, D_R = 10 $\mu m^2\ s^{-1}$; μ_S, μ_R = 0.3 s^{-1}; J_S, J_R = 0.3 mol s^{-1}; $\gamma = 4.5 \times 10^{-3}$ μm s^{-1} and $R_0 = 5 \times 10^{-4}$ mol.

The cell migration rate V_{cell} is a function of the amount of R present at the cell position, R_{cell}. The migration rates of many cell types have been found to have a biphasic response to cell substrate adhesiveness. Maximum cell velocity takes place at intermediate levels of adhesiveness (Schwartz & Horwitz, 2006).

We model this dependence with the following velocity response function:

$$V_{cell} = \gamma \cdot \frac{R_{cell}}{R_0} \cdot \exp\left(-\frac{R_{cell}}{R_0}\right)$$

R_0 is a characteristic concentration and γ is a constant that scales the velocity response. When $R_{cell}/R_0 \ll 1$, it corresponds to a situation where the cell has weak contact with the substrate and insufficient traction, while $R_{cell}/R_0 \gg 1$ corresponds to the cell adhering very strongly to the substrate. Deeper analysis of the model will be included in a follow-up publication.

Computer simulations

Simulations were carried out in MATLAB R2018a by iteratively applying the bvp5c boundary value problem solver. We assume that the reaction diffusion of signalling molecules S and R happens much faster than cell migration, such that the resulting distribution at each time step can be approximated by its steady-state solution. For each time step, R_{cell} is obtained through linear interpolation and used to calculate the cell position at the next step.

Data availability

This study includes no data deposited in external repositories.

Expanded View for this article is available online.

Acknowledgements
Work in the TJC and TES labs was funded by a Ministry Of Education of Singapore AcRF Tier 3 grant (MOE2016-T3-1-005). Work in the FL lab was supported by funding from the National Science Foundation, IOS-1354457. SMP is supported by Senior Research Fellowships (1042589 and 1156693) from the National Health and Medical Research Council of Australia. The work was assisted by the EMB Zebrafish Facility and EMB Imaging Facility, as well as the IMCB Zebrafish Facility.

Author contributions
Harsha Mahabaleshwar: Conceptualization; Formal analysis; Investigation. **PV Asharani:** Formal analysis; Investigation. **Tricia Yi Loo:** Conceptualization; Software; Formal analysis; Investigation; Methodology. **Shze Yung Koh:** Investigation. **Melissa R Pitman:** Formal analysis; Investigation; Writing—original draft. **Samuel Kwok:** Investigation. **Jiajia Ma:** Investigation. **Bo Hu:** Formal analysis; Investigation. **Fang Lin:** Supervision; Investigation. **Xue Li Lok:** Investigation. **Stuart M Pitson:** Conceptualization; Supervision; Writing—original draft. **Timothy Saunders:** Conceptualization; Supervision; Writing—original draft. **Tom Carney:** Conceptualization; Formal analysis; Supervision; Funding acquisition; Writing—original draft; Project administration; Writing—review & editing.

Disclosure and competing interests statement
The authors declare that they have no conflict of interest.

References

Bassett AR, Tibbit C, Ponting CP, Liu JL (2013) Highly efficient targeted mutagenesis of *Drosophila* with the CRISPR/Cas9 system. *Cell Rep* 4: 220–228

Blockus H, Chedotal A (2016) Slit-Robo signaling. *Development* 143: 3037–3044

Brend T, Holley SA (2009) Zebrafish whole mount high-resolution double fluorescent *in situ* hybridization. *J Vis Exp* 25: e1229

Burgess HA, Johnson SL, Granato M (2009) Unidirectional startle responses and disrupted left-right co-ordination of motor behaviors in robo3 mutant zebrafish. *Genes Brain Behav* 8: 500–511

Carney TJ, Feitosa NM, Sonntag C, Slanchev K, Kluger J, Kiyozumi D, Gebauer JM, Coffin Talbot J, Kimmel CB, Sekiguchi K *et al* (2010) Genetic analysis of fin development in zebrafish identifies furin and hemicentin1 as potential novel fraser syndrome disease genes. *PLoS Genet* 6: e1000907

Chance RK, Bashaw GJ (2015) Slit-dependent endocytic trafficking of the robo receptor is required for son of sevenless recruitment and midline axon repulsion. *PLoS Genet* 11: e1005402

Dahlem TJ, Hoshijima K, Jurynec MJ, Gunther D, Starker CG, Locke AS, Weis AM, Voytas DF, Grunwald DJ (2012) Simple methods for generating and detecting locus-specific mutations induced with TALENs in the zebrafish genome. *PLoS Genet* 8: e1002861

Fiore VF, Wong SS, Tran C, Tan C, Xu W, Sulchek T, White ES, Hagood JS, Barker TH (2018) alphavbeta3 Integrin drives fibroblast contraction and strain stiffening of soft provisional matrix during progressive fibrosis. *JCI Insight* 3: e97597

Fish JE, Wythe JD, Xiao T, Bruneau BG, Stainier DY, Srivastava D, Woo S (2011) A Slit/miR-218/Robo regulatory loop is required during heart tube formation in zebrafish. *Development* 138: 1409–1419

Fricke C, Lee JS, Geiger-Rudolph S, Bonhoeffer F, Chien CB (2001) astray, a zebrafish roundabout homolog required for retinal axon guidance. *Science* 292: 507–510

Geisler R (2002) Mapping and cloning, In *Zebrafish: a practical approach*, Nusslein-Volhard C, Dahm R (eds), pp 175–212. Oxford: Oxford University Press

Gros J, Hu JK, Vinegoni C, Feruglio PF, Weissleder R, Tabin CJ (2010) WNT5A/JNK and FGF/MAPK pathways regulate the cellular events shaping the vertebrate limb bud. *Curr Biol* 20: 1993–2002

Hinz B (2016) The role of myofibroblasts in wound healing. *Curr Res Transl Med* 64: 171–177

Hisano Y, Ota S, Takada S, Kawahara A (2013) Functional cooperation of spns2 and fibronectin in cardiac and lower jaw development. *Biol Open* 2: 789–794

Ho J, Tumkaya T, Aryal S, Choi H, Claridge-Chang A (2019) Moving beyond P values: data analysis with estimation graphics. *Nat Methods* 16: 565–566

Hobson JP, Rosenfeldt HM, Barak LS, Olivera A, Poulton S, Caron MG, Milstien S, Spiegel S (2001) Role of the sphingosine-1-phosphate receptor EDG-1 in PDGF-induced cell motility. *Science* 291: 1800–1803

Hofrichter MAH, Mojarad M, Doll J, Grimm C, Eslahi A, Hosseini NS, Rajati M, Müller T, Dittrich M, Maroofian R *et al* (2018) The conserved p.Arg108 residue in S1PR2 (DFNB68) is fundamental for proper hearing: evidence from a consanguineous Iranian family. *BMC Med Genet* 19: 81

Hopyan S, Sharpe J, Yang Y (2011) Budding behaviors: growth of the limb as a model of morphogenesis. *Dev Dyn* 240: 1054–1062

Hu H (2001) Cell-surface heparan sulfate is involved in the repulsive guidance activities of Slit2 protein. *Nat Neurosci* 4: 695–701

Jen JC, Chan WM, Bosley TM, Wan J, Carr JR, Rub U, Shattuck D, Salamon G, Kudo LC, Ou J *et al* (2004) Mutations in a human ROBO gene disrupt hindbrain axon pathway crossing and morphogenesis. *Science* 304: 1509–1513

Kanazawa S, Fujiwara T, Matsuzaki S, Shingaki K, Taniguchi M, Miyata S, Tohyama M, Sakai Y, Yano K, Hosokawa KO *et al* (2010) bFGF regulates

PI3-kinase-Rac1-JNK pathway and promotes fibroblast migration in wound healing. *PLoS One* 5: e12228

Kidd T, Bland KS, Goodman CS (1999) Slit is the midline repellent for the Robo receptor in *Drosophila*. *Cell* 96: 785–794

Kimmel CB, Ballard WW, Kimmel SR, Ullmann B, Schilling TF (1995) Stages of embryonic development of the zebrafish. *Dev Dyn* 203: 253–310

Kruszka P, Tanpaiboon P, Neas K, Crosby K, Berger SI, Martinez AF, Addissie YA, Pongprot Y, Sittiwangkul R, Silvilairat S *et al* (2017) Loss of function in ROBO1 is associated with tetralogy of Fallot and septal defects. *J Med Genet* 54: 825–829

Kupperman E, An S, Osborne N, Waldron S, Stainier DY (2000) A sphingosine-1-phosphate receptor regulates cell migration during vertebrate heart development. *Nature* 406: 192–195

Lau K, Tao H, Liu H, Wen J, Sturgeon K, Sorfazlian N, Lazic S, Burrows JTA, Wong MD, Li D *et al* (2015) Anisotropic stress orients remodelling of mammalian limb bud ectoderm. *Nat Cell Biol* 17: 569–579

Lee MJ, Van Brocklyn JR, Thangada S, Liu CH, Hand AR, Menzeleev R, Spiegel S, Hla T (1998) Sphingosine-1-phosphate as a ligand for the G protein-coupled receptor EDG-1. *Science* 279: 1552–1555

Lee RT, Knapik EW, Thiery JP, Carney TJ (2013) An exclusively mesodermal origin of fin mesenchyme demonstrates that zebrafish trunk neural crest does not generate ectomesenchyme. *Development* 140: 2923–2932

Liu KY, Sengillo JD, Velez G, Jauregui R, Sakai LY, Maumenee IH, Bassuk AG, Mahajan VB, Tsang SH (2018) Missense mutation in SLIT2 associated with congenital myopia, anisometropia, connective tissue abnormalities, and obesity. *Orphanet J Rare Dis* 13: 138

Lu W, van Eerde AM, Fan X, Quintero-Rivera F, Kulkarni S, Ferguson H, Kim H-G, Fan Y, Xi Q, Li Q-G *et al* (2007) Disruption of *ROBO2* is associated with urinary tract anomalies and confers risk of vesicoureteral reflux. *Am J Hum Genet* 80: 616–632

MacMullin A, Jacobs JR (2006) Slit coordinates cardiac morphogenesis in *Drosophila*. *Dev Biol* 293: 154–164

Martin P, Lewis J (1986) Normal development of the skeleton in chick limb buds devoid of dorsal ectoderm. *Dev Biol* 118: 233–246

Matsui T, Raya A, Callol-Massot C, Kawakami Y, Oishi I, Rodriguez-Esteban C, Izpisua Belmonte JC (2007) miles-apart-Mediated regulation of cell-fibronectin interaction and myocardial migration in zebrafish. *Nat Clin Pract Cardiovasc Med* 4(Suppl 1): S77–S82

Mendelson K, Lan Y, Hla T, Evans T (2015) Maternal or zygotic sphingosine kinase is required to regulate zebrafish cardiogenesis. *Dev Dyn* 244: 948–954

Mommersteeg MT, Yeh ML, Parnavelas JG, Andrews WD (2015) Disrupted Slit-Robo signalling results in membranous ventricular septum defects and bicuspid aortic valves. *Cardiovasc Res* 106: 55–66

Osborne N, Brand-Arzamendi K, Ober EA, Jin SW, Verkade H, Holtzman NG, Yelon D, Stainier DY (2008) The spinster homolog, two of hearts, is required for sphingosine 1-phosphate signaling in zebrafish. *Curr Biol* 18: 1882–1888

Oster GF, Murray JD, Harris AK (1983) Mechanical aspects of mesenchymal morphogenesis. *J Embryol Exp Morphol* 78: 83–125

Pitson SM (2011) Regulation of sphingosine kinase and sphingolipid signaling. *Trends Biochem Sci* 36: 97–107

Santiago-Martinez E, Soplop NH, Patel R, Kramer SG (2008) Repulsion by Slit and Roundabout prevents Shotgun/E-cadherin-mediated cell adhesion during *Drosophila* heart tube lumen formation. *J Cell Biol* 182: 241–248

Santos-Cortez R, Faridi R, Rehman A, Lee K, Ansar M, Wang X, Morell R, Isaacson R, Belyantseva I, Dai H *et al* (2016) Autosomal-recessive hearing impairment due to rare missense variants within S1PR2. *Am J Hum Genet* 98: 331–338

Satsu H, Schaeffer M-T, Guerrero M, Saldana A, Eberhart C, Hodder P, Cayanan C, Schürer S, Bhhatarai B, Roberts ED *et al* (2013) A sphingosine 1-phosphate receptor 2 selective allosteric agonist. *Bioorg Med Chem* 21: 5373–5382

Schwartz MA, Horwitz AR (2006) Integrating adhesion, protrusion, and contraction during cell migration. *Cell* 125: 1223–1225

Shen H, Giordano F, Wu Y, Chan J, Zhu C, Milosevic I, Wu X, Yao K, Chen BO, Baumgart T *et al* (2014) Coupling between endocytosis and sphingosine kinase 1 recruitment. *Nat Cell Biol* 16: 652–662

Thisse C, Thisse B (2008) High-resolution *in situ* hybridization to whole-mount zebrafish embryos. *Nat Protoc* 3: 59–69

Trinh LA, Stainier DY (2004) Fibronectin regulates epithelial organization during myocardial migration in zebrafish. *Dev Cell* 6: 371–382

van Eeden FJ, Granato M, Schach U, Brand M, Furutani-Seiki M, Haffter P, Hammerschmidt M, Heisenberg CP, Jiang YJ, Kane DA *et al* (1996) Genetic analysis of fin formation in the zebrafish, Danio rerio. *Development* 123: 255–262

Wada N (2011) Spatiotemporal changes in cell adhesiveness during vertebrate limb morphogenesis. *Dev Dyn* 240: 969–978

Wang F, Nobes CD, Hall A, Spiegel S (1997) Sphingosine 1-phosphate stimulates rho-mediated tyrosine phosphorylation of focal adhesion kinase and paxillin in Swiss 3T3 fibroblasts. *Biochem J* 324(Pt 2): 481–488

Wyngaarden LA, Vogeli KM, Ciruna BG, Wells M, Hadjantonakis AK, Hopyan S (2010) Oriented cell motility and division underlie early limb bud morphogenesis. *Development* 137: 2551–2558

Xiao T, Staub W, Robles E, Gosse NJ, Cole GJ, Baier H (2011) Assembly of lamina-specific neuronal connections by slit bound to type IV collagen. *Cell* 146: 164–176

Yamamura S, Hakomori S, Wada A, Igarashi Y (2000) Sphingosine-1-phosphate inhibits haptotactic motility by overproduction of focal adhesion sites in B16 melanoma cells through EDG-induced activation of Rho. *Ann N Y Acad Sci* 905: 301–307

Ye D, Lin F (2013) S1pr2/Galpha13 signaling controls myocardial migration by regulating endoderm convergence. *Development* 140: 789–799

Ye D, Xie H, Hu B, Lin F (2015) Endoderm convergence controls subduction of the myocardial precursors during heart-tube formation. *Development* 142: 2928–2940

Zhu W, Gliddon BL, Jarman KE, Moretti PAB, Tin T, Parise LV, Woodcock JM, Powell JA, Ruszkiewicz A, Pitman MR *et al* (2017) CIB1 contributes to oncogenic signalling by Ras via modulating the subcellular localisation of sphingosine kinase 1. *Oncogene* 36: 2619–2627

